Research

Check for updates

Author for correspondence:
Paul S. Fennell
e-mail: p.fennell@imperial.ac.uk

A three-interface random pore model: the reduction of iron oxide in chemical looping and green steel technologies

Jasper J. Wong[1], Diana Iruretagoyena[1], Nilay Shah[2] and Paul S. Fennell[1]

[1]Department of Chemical Engineering, and [2]Centre for Process Systems Engineering, Department of Chemical Engineering, Imperial College London, South Kensington Campus, London SW7 2AZ, UK

JJW, 0000-0003-1214-0353

Accurate modelling of the gaseous reduction of porous iron oxide powders or fines is important in industry for (i) reinventing the carbon intensive production of iron and steel and (ii) chemical looping technologies in the sphere of carbon capture and storage. A new three-interface random pore model is derived and applied to the gaseous reduction of hematite (Fe_2O_3) to iron (Fe). The structural reaction–diffusion model is able to describe three simultaneously reacting oxide layers, Fe_2O_3, magnetite (Fe_3O_4) and wustite (Fe_wO). The geometric nature of the model encodes structural information about the particles (porosity, surface area, pore length and size distribution), measured here by experiment. The model is usefully able to separate structural particle properties from individual rates of reaction and product layer diffusion. The results have been compared and fitted to thermogravimetric experiments between 800–1000°C and three CO/CO_2 gas mixtures. Rate constants for each indvidual reaction have been obtained and fit well to Arrhenius plots. The reduction of Fe_2O_3–Fe_3O_4 was controlled by diffusion and reaction kinetics, while the reduction of Fe_3O_4–Fe_wO and Fe_wO–Fe was limited by reaction kinetics. Metallization rates of the iron oxide powders

THE ROYAL SOCIETY
PUBLISHING

were rapid, showing promise for both hydrogen-based direct reduced iron and chemical looping processes.

1. . Introduction

This section provides the background motivation behind the new three-interface random pore model (RPM) that is developed in this paper (table 1).

(a) Decarbonization of iron and steel

Climate change demands the decarbonization of industrial carbon dioxide emissions. One such industrial source is iron and steel production, an extremely energy-intensive manufacturing industry. Steel is essential for human development and provides necessary structure in housing, public infrastructure, transport, energy infrastructure and the list goes on. However, the industry accounts for 2.6 $GtCO_2/y$, 30% of overall industrial CO_2 emissions and 7–9% of the total global CO_2 emissions [1,2]. Key to achieving lower emissions is how to chemically reduce iron oxide to iron without the use of carbonaceous fuels. The majority (greater than 70%) of iron is produced via the blast furnace and basic oxygen furnace (BF-BOF) route [3] with coke, derived from coal, used as the chemical reductant. The basic method of iron production has remained surprisingly similar, despite improvements in scale, efficiency and cost; some early blast furnaces have been recovered in Africa from 2900 BC, at the advent of iron and steel production. The co-production of carbon dioxide in the blast furnace accounts for the majority (70–90%) of emissions in iron and steelmaking [4].

Hydrogen gas (H_2) is an attractive alternative reductant to coke (being zero-carbon at the point of use) with potential to reduce CO_2 emissions in iron and steelmaking [5–7]. However, the production of hydrogen is currently dominated by steam methane reforming (SMR), being the most economically attractive (US\$ 2.31/kg H_2) and technologically mature process developed [6]. SMR relies on fossil fuel feedstocks and is energy intensive, resulting in 7 kg CO_2 per kg of H_2 produced. With carbon capture and storage (CCS), these emissions can be reduced but not eliminated; take for example 90% capture efficiency [8] and 67% thermal efficiency for conversion from a carbonaceous fuel [9], the steel industry emissions would reduce to approximately $(2.6 \times (1 - 0.9))/0.67 = 0.39$ $GtCO_2/y$, compared with the present 2.6 $GtCO_2/y$.

There are several projects and technologies aiming to reduce CO_2 emissions in iron and steelmaking. The HYBRIT project in Sweden is a direct reduced iron (DRI) process based on iron oxide pellets and hydrogen as the reductant. Electrolysis of iron oxide has also been explored by alkaline electrolysis (ULCOWIN) and molten oxide electrolysis (Boston Metals), but are not yet mature technologies. A comprehensive review of specific carbon emission reduction technologies in the global steel industry is provided here [10]. Flash reduction of small iron oxide fines (particles of sizes between 20 and 300 µm) are of particular interest to this work. Iron oxide fines are important in next generation low-carbon iron and steel production having recently been suggested for fast reaction times, high through-puts and without the need for energy-intensive pelletization processes, offering the potential for cost, energy carbon emission savings in new processes. Flash reduction technologies are being developed in the ZESTY process by Australian company CALIX Ltd and the Flash Ironmaking Technology (FIT) at Ohio State University [11,12]. At this particle scale, high conversions or metallization % may be obtained at residence times in the seconds, suitable for in-flight or flash reduction by methane, syngas or hydrogen feeds [5,11,12]. By contrast, the complete reduction of larger pellets ($d_p \sim 7$ mm, $\epsilon \sim 0.001$ to 0.005) commonly used in the industrial production of DRI is in the time scale of minutes or hours. The reduction processes of fines or powders are not modelled effectively by simple shrinking core models, which assume sharp reaction interfaces [6,13]. At small particle sizes and high porosity, reaction rates are rapid and internal reaction surface area become large compared with the external particle surface area. This reduces the applicability of these traditional modelling

Table 1. Nomenclature.

$\Delta H_{i,T}^{\circ}$	standard enthalpy of reaction i at temperature T	kJ mol^{-1}
ϵ	particle porosity	$(-)$
ϵ_0	initial particle porosity	$(-)$
$C_{Fe^{2+},i}$	concentrations of iron ions at the product/reactant interface for reaction i	mol m^{-3}
C_i	gaseous concentration driving force at the product/reactant interface for reaction i	mol m^{-3}
$C_{j,i}$	gaseous concentration for component $j = A, B$ at the product/reactant interface for reaction i	mol m^{-3}
$C_{O^{2-},j}$	concentrations of oxygen ions at the product/reactant interface for reaction j	mol m^{-3}
C_s	gaseous concentration driving force at the pore surface interface	mol m^{-3}
$D_{Fe^{2+},2}$	effective solid-state diffusivity of iron ions in wustite product layer	m^2 s^{-1}
$D_{Fe^{n+},1}$	effective solid-state diffusivity of ion in magnetite product layer	m^2 s^{-1}
D_i	effective gaseous diffusivity of reaction i	m^2 s^{-1}
$D_{O^{2-},3}$	effective solid-state diffusivity of oxygen ions in iron product layer	m^2 s^{-1}
$f(r)$	size distribution of non-overlapped cylinders at any time	$(-)$
J_i	diffusion flux through product layer i	mol m^{-2} s^{-1}
K_i	equilibrium constant for reaction i	$(-)$
$k_{s,i}$	diffusic rate constant based on rate of conversion per unit reaction interface area, for reaction i	m^4 mol^{-1} s^{-1}
L	total length of overlapped cylindrical system	m
L_E	total length of non-overlapped cylindrical system	m
m	shape factor	—
r_i'	virtual radius of cylindrical product layer surface for reaction i	m
R_i	reaction rate at the product/reactant interface for reaction i	mol m^{-2} s^{-1}
r_i	radius of cylindrical reaction surface for reaction i	m
S_0	reaction surface area at $t = 0$ of overlapped system, per unit volume	m^{-1}
$S_{E,i}$	surface area of non-overlapped cylindrical system, per unit volume for reaction interface i	m^{-1}
S_i	reaction surface area of overlapped system, per unit volume for reaction interface i	m^{-1}
t	reaction time	s
V_i'	virtual volume enclosed by non-overlapped product layer surface for reaction i, per unit particle volume	$(-)$
V_0	volume enclosed by non-overlapped reaction interface at $t = 0$ i per unit particle volume	$(-)$
$V_{E,i}$	volume enclosed by non-overlapped cylindrical system, per unit particle volume for reaction interface i	$(-)$
V_i	volume enclosed by non-overlapped reaction interface i per unit particle volume	$(-)$
$V_{m,i}$	molar volume of solid product formed by reaction i	m^3 mol^{-1}
w	ratio of Fe : 0 in wustite	$(-)$
X	overall solid conversion	$(-)$
X_i	solid conversion for reaction i	$(-)$
x_i	effective diffusion length in product layer i	m
Z_i	ratio of solid product molar volume to the solid reactant molar volume for reaction i	$(-)$

approaches developed for the iron and steel industry. The exact size at which this occurs depends on the multiple conditions and sample characteristics, such as gas composition, porosity, internal surface area and temperature, but previous studies at the 100–425 μm particle size range have deferred to alternative modelling approaches [13–17]. This creates a need for more accurate particle scale models that are applicable to next-generation, decarbonized iron and steelmaking processes.

(b) Chemical looping technologies for industrial decarbonization

The deployment of CCS in conjunction with other energy technologies (like renewables, nuclear) has received considerable attention with the dual aim of minimizing the cost of electricity supply and reducing CO_2 emissions [8]. Prominent CCS technologies include solvent/amine scrubbing, oxyfuel combustion, chemical and calcium looping, as well as less mature low-temperature adsorbents and ionic liquids and are discussed in detail here [8,18–20]. Chemical looping combustion in particular has been suggested as a promising alternative with inherent carbon dioxide capture and a low separation energy penalty [8,21–23].

Chemical looping processes are a family of promising technologies for decarbonized power generation, hydrogen production and have promising industrial synergy with iron, steel and cement production. Chemical looping involves redox cycling of metal-oxide particles (known as oxygen carriers), which provide the oxygen for the combustion of fossil fuels.

In the reducer, the metal oxide particles are reduced and oxidize a fuel gas to a mixture of CO_2 and H_2O. Since nitrogen or other gaseous components of air are not introduced to the combustion process, the by-product steam may be easily condensed and separated from the CO_2. In the oxidizer, the reduced metal-oxide carrier is re-oxidized or regenerated with air to produce a stream of hot vitiated air (for power generation or otherwise), and is returned to the reducer, completing the chemical loop. Importantly, the inherent nature of carbon dioxide separation means that no energy intensive processing or equipment are required. A detailed review of chemical looping has been provided in the literature [23].

Chemical looping water splitting (CLWS) has also been proposed for hydrogen production; in CLWS, the metal-oxide is partially re-oxidized in steam (producing hydrogen), instead of air. Clean hydrogen production is highly relevant to decarbonizing iron and steel, as previously discussed and an adaptation of CLWS has recently been suggested as an opportunity for the co-production of hydrogen and decarbonized iron [1,6,24].

The modelling of gas–solid reactions involved between process gases and the small metal oxide powders (100–425 μm) applicable in chemical looping are relevant to this paper, since the small particle size and high porosity and surface area mean traditional modelling approaches are not suitable [13,15–17]. In addition, iron oxide and iron-based metal oxide carriers have been studied as leading candidates in chemical looping applications [1,6,14,15]. To use the full oxygen capacity of the carriers, full reduction is required, meaning that the full development of multiple product layers is expected [1,6]. Because of this, modelling of the entire reduction process from Fe_2O_3 to Fe is important to accurately describe the reaction.

(c) Mathematical modelling of gas–solid reactions

Studies on the mathematical modelling of gas–solid reactions involving iron-oxide have included operation at lower temperatures [25,26], different CO/H_2 gas compositions [27], higher pressures [16], with iron oxide compacts [28,29], disks [30], pellets [31–34], ore fines [35–37] and across different stages of reduction [13,16,17]. Industrial gas–solid reaction modelling is detailed in [38]. Zero dimensional 'kinetic' models have also been developed to best fit experimental data, where arbitrary rate equations are defined by manipulating a range of adjustable parameters [14]. Mathematical modelling of gaseous reduction of iron oxides is reviewed in [39], and reduction by hydrogen summarized in [3].

The RPM is able capture diffuse reaction fronts and the evolution of pore structure [40,41]. This model, unlike the simpler shrinking core model, includes parameters that give information about the complex structure of the porous solid material. Moreover, idealized uniform pore/grain sizes that are present in the grain model are avoided, which enables random orientations of pores and distribution of pores sizes to be incorporated into the reaction model. Structural information about the particles, such as surface area, porosity and pore size distribution, are included in the model and are obtainable by experiment, thus enabling a more accurate and transferable reaction conversion model that separates the rates of interfacial reaction and product layer diffusion from the structural properties of the sample.

Until now, the RPM has been used to describe industrially relevant gas–solid reactions such as the carbonation of calcium oxide [42,43], char gasification [44–46] and combustion [47], and more recently, the reduction of iron oxides. However, it has been limited to describing a single reaction step or product layer systems, meaning its applicability has been severely restricted to the hematite-magnetite system [16] and the wustite-iron system [17] for iron oxides. Here, we derive a three-interface RPM. The three-interface RPM is a generalization of the RPM to include the growth of three simultaneously evolving product layers that are necessary to model to the reduction of Fe_2O_3 all the way to Fe. The model is based on the geometric evolution of reaction interfaces and product layers that are determined by structural parameters, reaction kinetics, product layer diffusion and the statistics of pore intersections. The model results fit well to reaction kinetics for the gaseous reduction of iron oxide obtained by TGA experiments, and also includes structural information obtained by nitrogen adsorption analysis, helium adsorption analysis and mercury intrusion porosimetry (MIP). This will allow more complete physics-based modelling of the gaseous reduction of iron oxide applied to either green or decarbonized iron production and chemical looping technologies for clean power generation or low-carbon hydrogen production.

This paper details in §2, experiments that are used to validate the (§3) theory and model formulation for the new three-interface RPM and, finally, in §4, the results are discussed, comparing modelling results with experiment and background literature.

2. Experiments

This section details material synthesis, TGA experiments and material characterization for validation of the three-interface RPM derived in this paper.

(a) Material synthesis

A batch of mechanically mixed (MM) Fe_2O_3 particles were prepared by mixing 0.2 mol of Fe_2O_3 (powder <5 m, >96% from Sigma Aldrich) with 30 ml of DI water. The slurry was loaded into a planetary ball mill (PM-400, RETSCH) and was milled together with steel balls for 6 h at 250 r.p.m. The sample was dried overnight at 60°C and calcined for 6 h at 900°C in air (2 min^{-1}) using a horizontal tube furnace with a heating rate of 15°C min^{-1} and sieved ($d_p \sim 150$ to 300 μm).

(b) TGA experiments

The gaseous reduction of iron oxide (Fe_2O_3, $d_p \sim 150$ to 300 μm, MM, Sigma Aldrich) was experimentally investigated by TGA analysis (TA Instruments, Q5000). The TGA consists of a high-precision balance within a furnace, with temperature and sample/balance gas flows controlled by the TGA software and two internal mass flow controllers (MFCs). The external gas supply was controlled by an in-house Agilent Vee program and three external MFCs (Bronkhurst), connected to a computer running the TGA software using a multi-channel P.C. system. The iron oxide sample (5 mg) is loaded on a platinum pan and is transported into the TGA using the autosampler, which has the capability to run multiple consecutive samples (25 sample capacity). Gases were supplied from cylinders of (i) pure N_2 (99.998 vol %, oxygen-free, BOC), (ii) 30 vol % CO (balance N_2, BOC) and (iii) 99.9% CO_2, (BOC); desired gas compositions from these cylinders

were achieved via programming of the MFCs. A total flow rate of 200 ml min^{-1} was set for all experiments. The external MFC control programs and the TGA were synchronized using a USB data asquisition module (Measurement Computing USB-1208FS) and the output signal function of the TGA.

(c) Characterization experiments

The structures of the solid samples were examined by scanning electron microscopy (SEM, JOEL 5800LV), mercury-intrusion porosimetry (Micromeritics, Autopore IV), N_2 adsorption analysis (Micromeritics, Tristar 3000) and helium adsorption analysis (Micromeritics, AccuPyc 1330). For SEM, the solid samples were sputter-coated by a thin layer (thickness less than 100 nm) of gold, before being examined under a vacuum (less than 1 mbar) with an accelerating voltage of 15 kV. The pore size distribution (7 nm $< d_{pore} < 0.20$ mm) of particles of Fe_2O_3 was measured by a mercury porosimeter at 298 K. For N_2 and helium adsorption analysis, the data from N_2 and helium isotherms were used to calculate the specific surface area (employing the Brunauer–Emmett–Teller (BET) method) and skeletal density, respectively.

3. Theory and model formulation

This section describes the RPM, the iron oxide reaction system and derives and solves the new three-interface RPM developed in this paper.

(a) The random pore model

The original RPM describes the reaction between a gas and a solid particle to form a gas and a porous solid product, with similar chemical and physical processes to those widely understood in the shrinking core model. The difference lies in the physical description of the porous particle; the pores are described as a collection of overlapping cylinders (or any shape, described by the shape factor m) [40,41]. The orientation and position of these cylinders is random, but the total size of the particle, and number and length of the pores, remains constant during the course of the reaction. Therefore, differences in molar volume between the reactant and product solid cause an increase in porosity, in the case of iron oxide reduction. The solid product also remains continuously connected, which affects the resultant morphology [17]. The reaction zone and overlapping of pores described by the RPM are depicted in figure 1, reproduced from [41].

In the RPM's formulation, a porous product layer is formed on the wall of a reactant pore. Depending on the gas–solid reaction system of the model, there is diffusion by gaseous molecules or solid-state ions across the product layer, and a reaction occurs at the gas–solid interface or at the reactant/product layer interface, where the result is oxidation of the reducing gas and reduction of the solid oxygen carrier. The reaction interface expands and the layer of product is thickened, increasing the resistance to diffusion. As the reaction interface expands, the reaction interfaces begin to overlap with other interfaces, but the number of pores and interfaces remains constant. So, while the reactive surface area increases due to the radial expansion of the interfaces, the overlap space between the initially separated interfaces begins to remove the reactive surface area. This is characterized by a rate maximum in the RPM's solution, which has been successfully observed and fitted to experimental data for single-step iron oxide reduction [15–17]. These studies have considered product layer reaction–diffusion mechanisms including gaseous diffusion of fuel gas [15,16], solid-state diffusion of iron ions [15,16] and diffusion of oxygen atoms [17].

Changes in molar volumes between the reactant and product solids are also included in the model, another valuable characteristic of the RPM. When the molar volume of the product is less than the reactant, the pore itself also expands radially. If the molar volume of the product is more, the pore will contract. For example, the molar volume of iron is 0.563 times that of wustite, so pore expansion is predicted. The dynamics of the geometry in turn impact the associated reaction
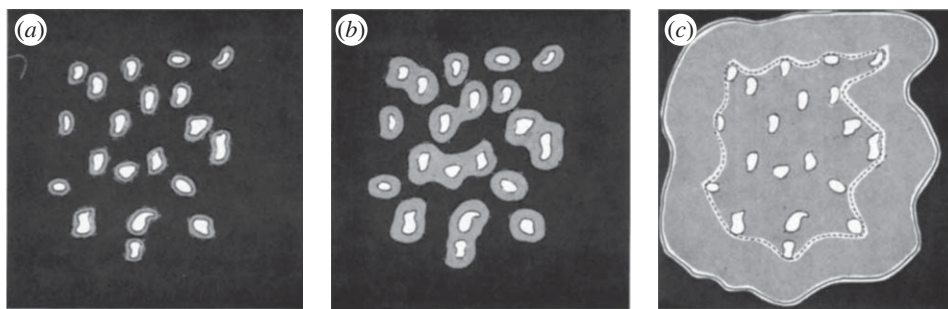
Figure 1. Two-dimensional depiction of overlapping pores in the original random pore model reproduced from [41]. The blackened area represents unreacted solid and the grey area represents the product layer. (*a*) Early stage without pore overlap, (*b*) intermediate stage with some overlapping of pores, (*c*) later stage with full product layer development and significant overlap.
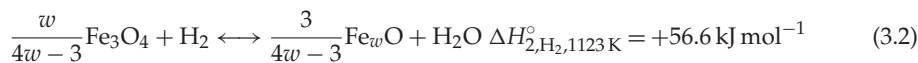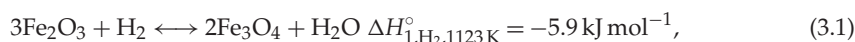
rates. SEM images (see the electronic supplementary material) show changes in the pore structure between the different iron oxides in the reduction process. Samples of different reduction extents were obtained at the end of TGA experiments at different CO/CO_2 reducing atmospheres, which controlled the thermodynamic reduction extent of each sample.

Characteristic parameters describing the initial structure of the particle that are required in the RPM are also easily measured using established experimental procedures such as mercury porosimetry, helium pycnometry and N_2 physisorption, meaning structure information about the sample easily obtainable via experiment may be separated from the diffusic rates of reaction and product layer diffusion.
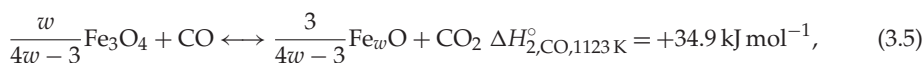
The general form of the model includes four modes of resistance: (1) resistance to external bulk mass transfer, (2) resistance to intra-particle diffusion, (3) resistance to product layer diffusion and (4) chemical reaction resistance. Commonly one form of resistance dominates, so it is unnecessary to consider all modes.

(b) Iron oxide reaction system

Accurate modelling of the reduction/oxidation of iron oxide particles requires an appreciation of the several oxidation states of the iron-based oxygen carriers: hematite (Fe_2O_3), magnetite (Fe_3O_4), wustite (Fe_wO), where $w = 0.947$ and metallic iron (Fe). The reduction reactions between these oxidation states for H_2 fuel gas are given [17] by

$$3Fe_2O_3 + H_2 \longleftrightarrow 2Fe_3O_4 + H_2O \; \Delta H^\circ_{1,H_2,1123\,K} = -5.9\,\text{kJ mol}^{-1}, \tag{3.1}$$

$$\frac{w}{4w-3}Fe_3O_4 + H_2 \longleftrightarrow \frac{3}{4w-3}Fe_wO + H_2O \; \Delta H^\circ_{2,H_2,1123\,K} = +56.6\,\text{kJ mol}^{-1} \tag{3.2}$$

and
$$Fe_wO + H_2 \longleftrightarrow wFe + H_2O \; \Delta H^\circ_{3,H_2,1123\,K} = -16.9\,\text{kJ mol}^{-1}. \tag{3.3}$$

For CO fuel gas, the reactions are given [17] by

$$3Fe_2O_3 + CO \longleftrightarrow 2Fe_3O_4 + CO_2 \; \Delta H^\circ_{1,CO,1123K} = -40.8\,\text{kJ mol}^{-1}, \tag{3.4}$$

$$\frac{w}{4w-3}Fe_3O_4 + CO \longleftrightarrow \frac{3}{4w-3}Fe_wO + CO_2 \; \Delta H^\circ_{2,CO,1123\,K} = +34.9\,\text{kJ mol}^{-1}, \tag{3.5}$$

$$Fe_wO + CO \longleftrightarrow wFe + CO_2 \; \Delta H^\circ_{3,CO,1123K} = -16.6\,\text{kJ mol}^{-1}. \tag{3.6}$$

Under mixtures of H_2/H_2O or CO/CO_2, these reactions are reversible. Figure 2*a*,*b* below shows iron oxide phase equilibria for CO/CO_2 and H_2/H_2O systems, respectively, where thermochemical data has been extracted from [48].
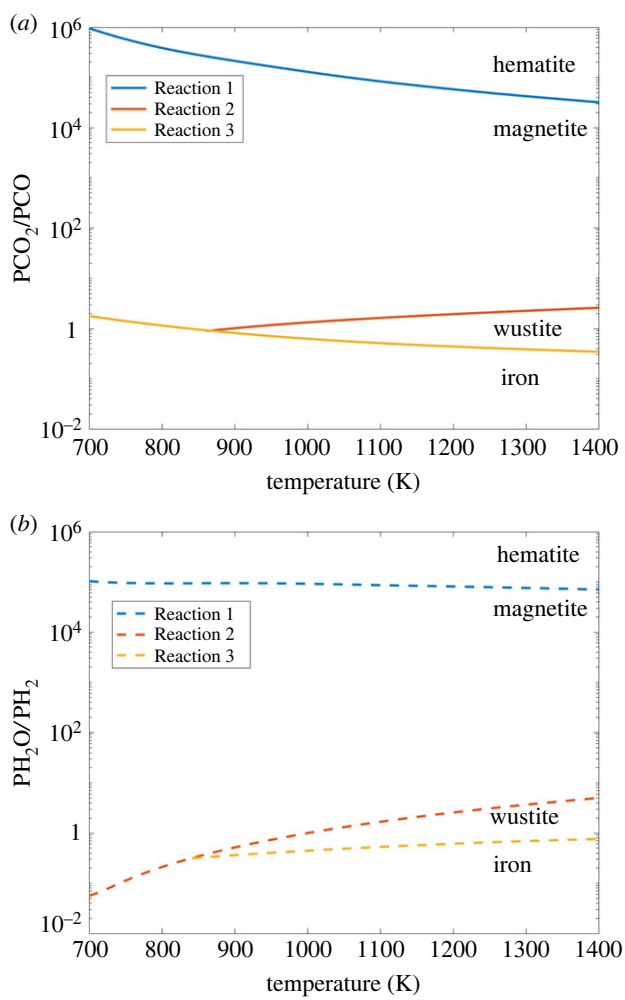
Figure 2. Equilibrium plots of iron oxide and (*a*) CO/CO$_2$ and (*b*) H$_2$/H$_2$O systems.

Although the principles apply for both CO or H$_2$, the following derivation is performed for a single fuel gas. This may be generalized to fuel gases containing mixtures of CO/H$_2$ by summing reaction rates for each gas, assuming they proceed independently of each other [31]. In a mixture of CO/H$_2$, an extra equation to account for the water-gas shift reaction would also be required in the numerical solver. To more simply show the development of the new three-interface RPM, the extensions that accompany modelling of syngas fuel mixtures have been omitted here.

(c) Three interface system: interfacial concentrations

In the original RPM, gaseous reactant is assumed to diffuse through the porous product layer driven by a linear concentration gradient and constant diffusivity D_s [40,41]. The diffusion flux J is written as

$$J = \frac{D_s}{x}(C_s - C_i), \tag{3.7}$$

where C_s and C_i are the reactant gas concentrations at the gas/solid product surface and solid product/solid reactant interface i, respectively, and x is the effective diffusion length across the product layer. In the RPM, the diffusion length is defined as the closest distance separating the reaction surface (at the product/reactant interface) from the surface of the pores. In a fully
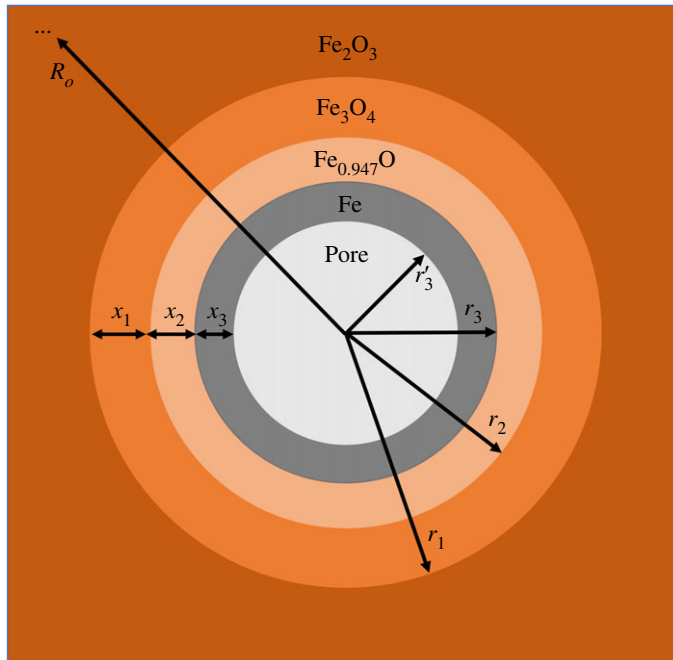
Figure 3. Two-dimensional depiction of one fully developed cylindrical pore in the three-interface random pore model.

developed three-layer system, however, we expect three product layers forming on the surface of a pore, complicating the model. A depiction of a fully developed pore in the three-layer RPM is shown in figure 3. The overlapping of pores proposed in [41] is depicted in figure 1.

A key determination in the three-interface RPM is calculation of interfacial gaseous concentrations $C_{j,i}$ using the quasi-steady-state approximation, where each interface is considered as stationary at any time. In $C_{j,i}$, i denotes index of the reaction interface, and the index $j = A, B$ represents $j = H_2, H_2O$ or $j = CO, CO_2$. The molar fluxes of gases through the product layers ($J_{j,i}$) and the interfacial reaction rates (R_i) are represented diagrammatically in figure 4 using a series–parallel electrical circuit analogy. Through each product layer of Fe, Fe_wO and Fe_3O_4, there are fluxes for component $j = A, B$ described by

(3) Fe layer

$$J_{j,3} = \frac{D_3}{x_3}(C_{j,s} - C_{j,3}), \tag{3.8}$$

(2) Fe_wO layer

$$J_{j,2} = \frac{D_2}{x_2}(C_{j,3} - C_{j,2}), \tag{3.9}$$

(1) Fe_3O_4 layer

$$J_{j,1} = \frac{D_1}{x_1}(C_{j,2} - C_{j,1}). \tag{3.10}$$

At each reaction interface $i = 1, 2, 3$, there is a reaction described by

(3) Fe/Fe_wO interface

$$R_3 = \frac{k_{s,3}}{V_{m,3}}\left(C_{A,3} - \frac{C_{B,3}}{K_3}\right), \tag{3.11}$$

(2) Fe_wO/Fe_3O_4 interface

$$R_2 = \frac{4w - 3}{w}\frac{k_{s,2}}{V_{m,2}}\left(C_{A,2} - \frac{C_{B,2}}{K_2}\right), \tag{3.12}$$
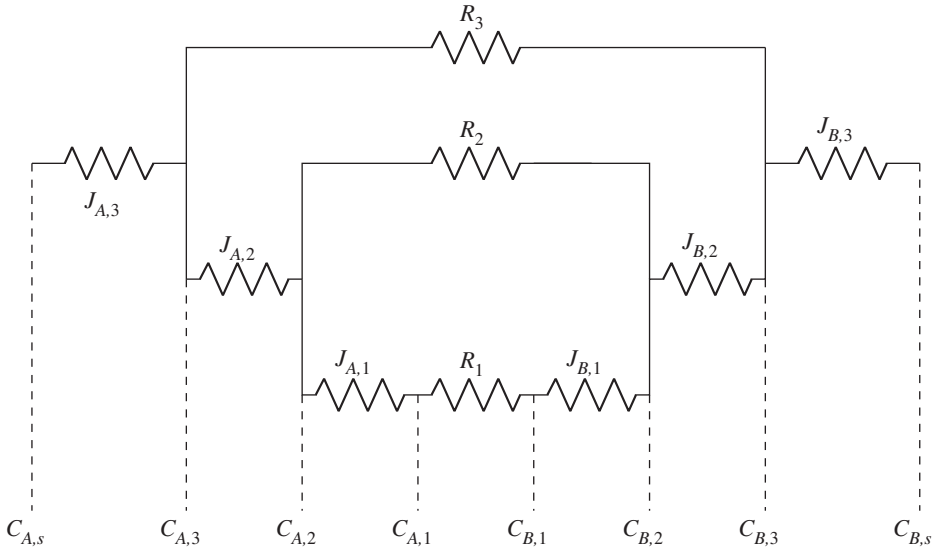
Figure 4. Electrical circuit analogy of the three-layered random pore model representing series–parallel resistances of interfacial reaction and product layer diffusion from the surface of a pore.

(1) Fe_3O_4/Fe_2O_3 interface

$$R_1 = \frac{k_{s,1}}{3V_{m,1}}\left(C_{A,1} - \frac{C_{B,1}}{K_1}\right),\tag{3.13}$$

where R_i is the reaction rate at interface i (mol m^{-2} s^{-1}), $k_{s,i}$ is the intrinsic rate constant (m^4 mol^{-1} s^{-1}) at the reaction interface i, K_i is the equilibrium constant for the reaction i and $V_{m,i}$ is the molar volume of the solid product formed by reaction i. The model describes a flux of reactant gas diffusing through the Fe product layer on the surface of an intra-particle pore at rate $J_{j,3}$. The reactant gas meets a parallel junction at the Fe/Fe$_w$O interface (3), where the gas reacts to thicken the Fe product layer, or diffuses through the next Fe$_w$O product layer. Performing a molar flux balance at the interface (3), we obtain

$$J_{A,3} = J_{A,2} + R_3.\tag{3.14}$$

The reactant gas diffusing through the Fe$_w$O product layer again meets a parallel junction at the Fe$_w$O/Fe$_3$O$_4$ interface (2), where the gas reacts to thicken the Fe$_w$O product layer or diffuses through the next Fe$_3$O$_4$ product layer. Performing a molar flux balance at the interface (2), we obtain

$$J_{A,2} = J_{A,1} + R_2.\tag{3.15}$$

The reactant gas diffusing through the Fe$_w$O product layer simply reacts at the Fe$_3$O$_4$/Fe$_2$O$_3$ interface (1). Performing a molar flux balance at the interface (1), we obtain

$$J_{A,1} = R_1.\tag{3.16}$$

Reactions in equations (3.1)–(3.6) demonstrate that the reactions occurring imply equimolar counter-diffusion, so that also imposes that the flux of reactant gas in through each product layer is equal to the flux of product gas back out, for $i = 1, 2, 3$

$$J_{A,i} = -J_{B,i}.\tag{3.17}$$

Together, these balances form a system of six simultaneous algebraic equations. In solving them, we may obtain expressions for interfacial gaseous concentrations in terms of interfacial radii. These will be input into the governing rate equations that are derived next.

(d) Three interface system: generalization of the random pore model

There are complexities in the formulation of the RPM that are introduced by gas solid reaction systems with more than one elementary reaction. This is true in the case of iron oxide reduction, where multiple product layers develop with coupled interfacial concentrations. It is expected that multiple-interface reaction systems often also contain solid product layers with different molar volumes because the RPM imposes the assumption of a constant overall particle size during the reaction. For iron oxide, three product layers are expected to develop simultaneously (provided the ratio of reducing gas to oxidizing gas is sufficiently high), as depicted in figure 3. In the original RPM, the reaction surface may be considered to be the resultant surface of a set of randomly overlapping cylindrical surfaces of size distribution $f(r)$ [40]. Here, $f(r)\,dr$ is the total length of the cylindrical surfaces (per unit volume of space) with radii between r and $r + dr$. The total length of the non-overlapped cylindrical system (per unit volume of space) is defined as

$$L_E = \int_0^\infty f(r)\,dr. \tag{3.18}$$

The total surface area of the non-overlapped cylindrical system is defined as

$$S_E = 2\pi \int_0^\infty r f(r)\,dr. \tag{3.19}$$

Finally, the total enclosed volume by the non-overlapped cylindrical system is defined as

$$V_E = \pi \int_0^\infty r^2 f(r)\,dr. \tag{3.20}$$

Assuming the number of cylinders remains constant, a balance over the size distribution of these cylinders gives

$$\frac{\partial f}{\partial t} + \frac{\partial}{\partial r}\left[f \frac{dr}{dt}\right] = 0, \tag{3.21}$$

which is equivalent to

$$\frac{\partial f}{\partial t} = -\frac{dr}{dt} \cdot \frac{\partial f}{\partial r}. \tag{3.22}$$

The original RPM assumes the rate of reaction is first order with respect to gaseous reactant and proportional to surface area

$$\frac{dV}{dt} = k_s C_i S, \tag{3.23}$$

which may also be written in terms of the rate of growth of the radius of the cylinders,

$$\frac{dr}{dt} = \frac{1}{S}\frac{dV}{dt} = k_s C_i. \tag{3.24}$$

Here, V is the volume enclosed by the reaction surface per unit volume of space, S is the reaction surface area per unit volume of space (m^{-1}), C_i is the concentration of gaseous reactant at the interface of the solid product/reactant and k_s is the rate constant for the surface reaction ($m^4\,mol^{-1}\,s^{-1}$). The original RPM derives rate equations based on irreversible reactions. In this system, we are dealing with reversible reactions, as evident in (3.11), (3.12) and (3.13). To simplify the derivation, we make the substitution $C_i = C_{A,i} - (C_{B,i}/K_i)$. So, we consider C_i as the concentration driving force for the forward reaction. Equations (3.23) and (3.24) in the original RPM are true for the first reaction from hematite to magnetite, giving

$$\frac{dV_1}{dt} = k_s C_1 S_1 \tag{3.25}$$

and

$$\frac{dr_1}{dt} = k_{s,1} C_1. \tag{3.26}$$

There are two key deviations from the original RPM in a three-interface system: (1) since the concentration driving force at the solid product/reactant interface is no longer constant in

time, equation (18) that is written in the original RPM does not apply, since $k_s C_i$ cannot be analytically integrated as done in the original derivation (C_i is not a constant). Expressions for C_i must be included in the governing differential equations (derived next), which must be solved numerically; and (2) in a three interface system with product layers of different molar volumes, dV_i/dt for subsequent product layers is not simply $k_{s,i} C_i S_i$. This can be understood if we consider that hematite initially reacts to form a thin layer of magnetite. Since magnetite has a greater molar volume than hematite, the product/gas interface will initially shrink radially by a virtual volume governed by (see the electronic supplementary material for details)

$$\frac{dV_1'}{dt} = (1 - Z_1)\frac{dV_1}{dt},\tag{3.27}$$

where $Z_1 = 1.49$ is the ratio of the solid product molar volume to the solid reactant molar volume, for Reaction 1 [49]. In general, the virtual volume is defined as the volume enclosed by the product/reactant interface from which the subsequent reaction proceeds. In other terms, this is the volume enclosed by the preceding reaction product layer if we suppose there is no successive reaction. The volume is referred to as virtual because it is proposed that the magnetite/gas interface simultaneously begins to react to form another layer of wustite by growing into the magnetite layer from the inside of the pore. This decreases the thickness of the magnetite layer and increases the rate of change of the innermost volume of the magnetite layer by an additional amount $k_{s,2} C_2 S_2$ compared with the virtual dV_1'/dt. The real volume of the second reaction interface is governed by

$$\frac{dV_2}{dt} = \frac{dV_1'}{dt} + k_{s,2} C_2 S_2 = (1 - Z_1)\frac{dV_1}{dt} + k_{s,2} C_2 S_2.\tag{3.28}$$

Conversely, Reaction 2 produces a layer of wustite product that expands (instead of shrinks) the pore size radially, due to the lower molar volume of wustite compared with magnetite. The virtual volume of the second product layer is governed by (see the electronic supplementary material for details)

$$\frac{dV_2'}{dt} = Z_2(1 - Z_1)\frac{dV_1}{dt} + (1 - Z_2)\frac{dV_2}{dt},\tag{3.29}$$

where $Z_2 = 0.27$ is the ratio of the solid product molar volume to the solid reactant molar volume, for Reaction 2 [49]. It is proposed that the wustite/gas interface will also begin to react to form a layer of iron by growing into the wustite layer from the inside of the pore. This decreases the thickness of the wustite layer and increases the real rate of change of volume enclosed by the innermost radius of the wustite layer by an additional amount $k_{s,3} C_3 S_3$ compared with the virtual dV_2'/dt. The real volume of the third reaction interface is thus governed by

$$\frac{dV_3}{dt} = \frac{dV_2'}{dt} + k_{s,3} C_3 S_3 = (1 - Z_1)\frac{dV_1}{dt} + (1 - Z_2)\frac{dV_2}{dt} + k_{s,3} C_3 S_3.\tag{3.30}$$

Finally, Reaction 3 produces an iron product that also expands the pore size radially due to the lower molar volume of iron compared with wustite. The virtual volume of the third product layer is governed by (see the electronic supplementary material for details)

$$\frac{dV_3'}{dt} = Z_3 Z_2(1 - Z_1)\frac{dV_1}{dt} + Z_3(1 - Z_2)\frac{dV_2}{dt} + (1 - Z_3)\frac{dV_3}{dt},\tag{3.31}$$

where $Z_3 = 0.57$ is the ratio of the solid product molar volume to the solid reactant molar volume, for Reaction 3 [49]. It is important to note that the third virtual volume V_i' is equal to the real volume, since there are no successive reactions growing into the product layer of iron.

Because of pore intersections, the interface radii do not simply scale with enclosed volume. So, governing equations for interfacial radii must also be defined in terms of enclosed volume and reaction surface area, using equation (3.24)

$$\frac{dr_1}{dt} = \frac{1}{S_1}\frac{dV_1}{dt}, \tag{3.32}$$

$$\frac{dr_2}{dt} = \frac{1}{S_2}\frac{dV_2}{dt} \tag{3.33}$$

and

$$\frac{dr_3}{dt} = \frac{1}{S_3}\frac{dV_3}{dt}. \tag{3.34}$$

Expressions for C_1, C_2 and C_3 present in the governing equations are obtained by solving equations (3.14), (3.15), (3.16) and (3.17) and also using $x_1 = (r_1 - r_2), x_2 = (r_2 - r_3)$ and $x_3 = (r_3 - r'_3)$. It remains to derive expressions for S_j, for which we rely on the geometry of the assumed cylindrical pore system and the statistics of pore intersections and subsequent overlap. Equation (3.22) may be generalized to represent an expression for the size distribution of the set of cylinders for the product reactant interface of each reaction $i = 1, 2, 3$

$$\frac{\partial f_i}{\partial t} = -\frac{dr_i}{dt} \cdot \frac{\partial f_i}{\partial r_i}. \tag{3.35}$$

If we apply the conditions $f(0) = f(\infty) = 0$, integrate equation (3.35) with respect to r and use the Leibniz integral rule, we yield

$$\frac{dL_{E,i}}{dt} = 0. \tag{3.36}$$

If equation (3.35) is multiplied by $2\pi r$, again integrated with respect to r (Leibniz integral rule), and combined with the definitions in equations (3.19) and (3.18), we get

$$\frac{dS_{E,i}}{dt} = 2\pi L_{E,i}\frac{dr_i}{dt}. \tag{3.37}$$

Applying a similar strategy, if equation (3.35) is multiplied by πr^2 and integrated with respect to r (Leibniz integral rule), we yield

$$\frac{dV_{E,i}}{dt} = S_{E,i}\frac{dr_i}{dt}. \tag{3.38}$$

If equation (3.37) is divided by equation (3.38) and integrated with respect to V, we get

$$S_{E,i} = \sqrt{S_{E0}^2 + 4\pi L_{E0}(V_E - V_{E0})}. \tag{3.39}$$

Here, initial conditions $S_{E,i} = S_{E0}$ and $V_{E,i} = V_{E0}$ at $t = 0$ have been applied. Equation (3.39) in this work is identical to equation (17) written in the original RPM [40], but it now represents the surface area enclosed by the product/reactant interface for each reaction i, instead of one interface. The non-overlapped cylindrical system may be related to the overlapped system by applying the same method as equations (19)–(27) in the original RPM, which is followed here. Avrami (1940) showed that increment in growth of the enclosed overlapped system volume is a fraction of the enclosed non-overlapped system [50]. This fraction is $(1 - V_i)$, the fractional volume of space occupied by unreacted solid

$$dV_i = (1 - V_i)\,dV_{E,i}. \tag{3.40}$$

This assumes the reaction is initiated at a large number of discrete nuclei that overlap as they grow [40] and is applicable here, where the reaction surface starts with an large system of reaction

surfaces suitable for nucleation. Because the rate of reaction is assumed to be proportional to surface area, we have

$$dV_i = S_i \frac{dr_i}{dt} dt \tag{3.41}$$

and

$$dV_{E,i} = S_{E,i} \frac{dr_i}{dt} dt. \tag{3.42}$$

Combined with equation (3.40), these yield

$$S_i = S_{E,i}(1 - V_i). \tag{3.43}$$

Since $V_i \to 0$ when $V_{E,i} \to 0$, integration of equation (3.40) yields

$$V_i = 1 - \exp(-V_{E,i}). \tag{3.44}$$

The change in total length of the overlapped system due to additional intersections over the increase in volume increment dV is given in [40]

$$dL_i = -\frac{L_i}{(1 - V_i)} dV_i. \tag{3.45}$$

Since there is zero overlap at $V = 0$, we have the condition that $\lim_{V \to 0} L = L_E$. Therefore, equation (3.45) may be integrated to give

$$L_J = L_{E,i}(1 - V_i). \tag{3.46}$$

Combining equations (3.44), (3.43), (3.46) and (3.39), we can obtain an expression for the reaction surface area per unit volume of space

$$S_i = S_0 \left(\frac{1 - V_i}{1 - V_0} \right) \sqrt{1 - \frac{4\pi L_0 (1 - V_0)}{S_0^2} \log\left(\frac{1 - V_i}{1 - V_0} \right)}. \tag{3.47}$$

Explicit expressions for r_i in terms of V_i may now be derived by taking the integral of

$$\frac{dV_i}{dr_i} = \frac{dV_i/dt}{dr_i/dt} = S_i = S_0 \left(\frac{1 - V_i}{1 - V_0} \right) \sqrt{1 - \frac{4\pi L_0 (1 - V_0)}{S_0^2} \log\left(\frac{1 - V_i}{1 - V_0} \right)}, \tag{3.48}$$

where $r_i = r_0$ and $V_i = V_0$ (V_0 here is equivalent to the initial particle porosity ϵ_0) at $t = 0$. This holds for all three reactions. This gives (see the electronic supplementary material for details)

$$r_i = r_0 + \frac{2(1 - \epsilon_0)}{S_0 \psi} \left(\sqrt{1 - \psi \log\left(\frac{1 - V_i}{1 - \epsilon_0} \right)} - 1 \right). \tag{3.49}$$

This expression completes the governing equations. Equation (3.25), (3.28) and (3.30) may be solved for the enclosed volumes of the three interfaces V_1, V_2 and V_3, together with equation (3.14), (3.15), (3.16) and (3.17) for interfacial concentration driving forces C_1, C_2, C_3 and equation (3.47) for the reaction surface area S_i. The initial conditions are

$$V_i = V_0 = \epsilon_0 \quad \text{at } t = 0 \tag{3.50}$$

and

$$r_i = r_0 \quad \text{at } t = 0. \tag{3.51}$$

The Symbolic Math Toolbox (MATLAB) was used to obtain explicit expressions for C_i. With these expressions, the numerical solver ode45 (MATLAB) was employed to obtain solutions to the coupled governing differential equations for enclosed volumes of each reaction interface. With enclosed volumes, conversions for each individual oxide X_1, X_2 and X_3 and the overall conversion X may be calculated (see the electronic supplementary material).

Previous work has shown that external and intraparticle heat and mass transport for oxygen carrier particles of size less than 300 μm under similar reaction conditions can be assumed to have negligible effects on the overall rate of reaction [15,51,52], which is also assumed for the derivation of this model. Additional resistances to mass transfer may readily be added in series to this reaction–diffusion model in situations where this is not the case.

Table 2. Experimental parameters included in the three-interface RPM.

parameter	value	units	experimental method
ϵ_0	0.22	—	MIP, helium adsorption
ρ_{skel}	5297	kg m^{-1}	helium adsorption
$L_0/10^{13}$	2.09	m m^{-3}	MIP
$S_0/10^6$	7.12	m^2 m^{-3}	BET
ψ	4.0	—	MIP, helium adsorption, BET analysis

4. Results

This section details experimental parameter estimation and discusses model results with respect to experiment and relevant literature.

(a) Experimental parameter estimation

Key to the RPM is the incorporation of a structural parameter ψ, which encodes information about initial internal pore structure of the solid particles. The structural parameter is given by

$$\psi = \frac{4\pi L_0(1 - \epsilon_0)}{S_0^2}. \tag{4.1}$$

S_0 may be calculated from BET pore surface area measurements, estimated experimentally via N_2 adsorption analysis (Micromeritics, Tristar 3000).

$$S_0 = S_g \rho_{\mathrm{env}}, \tag{4.2}$$

where $\rho_{\mathrm{env}} = \rho_{\mathrm{skel}}(1 - \epsilon_0)$. Here, the skeletal density is obtained from helium adsorption analysis (Micromeritics, AccuPyc 1330). The particle porosity ϵ_0 is obtained from the ratio between the pore volume V_p and the total particle volume $V_p + V_{\mathrm{skel}}$

$$\epsilon_0 = \frac{V_p}{V_p + V_{\mathrm{skel}}} = \frac{V_p}{V_p + \frac{1}{\rho_{\mathrm{skel}}}}. \tag{4.3}$$

The pore volume was obtained experimentally via MIP measurements (Micromeritics, Autopore IV).

$$L_0 = \frac{1}{\pi V_p} \int_0^{r_{\max}} \frac{v_0}{r^2} \, \mathrm{d}r. \tag{4.4}$$

Table 2 summarizes the estimated parameters from MIP, BET and helium adsorption measurements.

(b) Model results

The three-interface RPM was fitted to 15 TGA experiments at five temperatures between the range of 800–1000°C, and three gaseous concentrations of CO/CO$_2$ mixtures. A nonlinear least-squares approach was used to fit the model to experimental data via the trust-region-reflective algorithm in MATLAB. In addition to the experimental parameters, the three-interface RPM incorporates rate constants and diffusion coefficients for each reaction. This means the overall reduction includes six fitting constants. To separate individual reaction steps, the experiments were carefully designed, exploiting the thermodynamics of each reaction. Therefore, confidence intervals resultant from the model fitting procedure could be kept to a acceptable range. For example, the model was first fitted to experiments at 3% CO and 15% CO$_2$, to yield the rate constants $k_{s,1}$ and diffusion coefficients D_1 for the reduction of Fe$_2$O$_3$ to Fe$_3$O$_4$. Figure 5a shows an example fit for Reaction 1 (R1) at $T = 900$°C. The obtained parameters for $k_{s,1}$ and D_1 were then
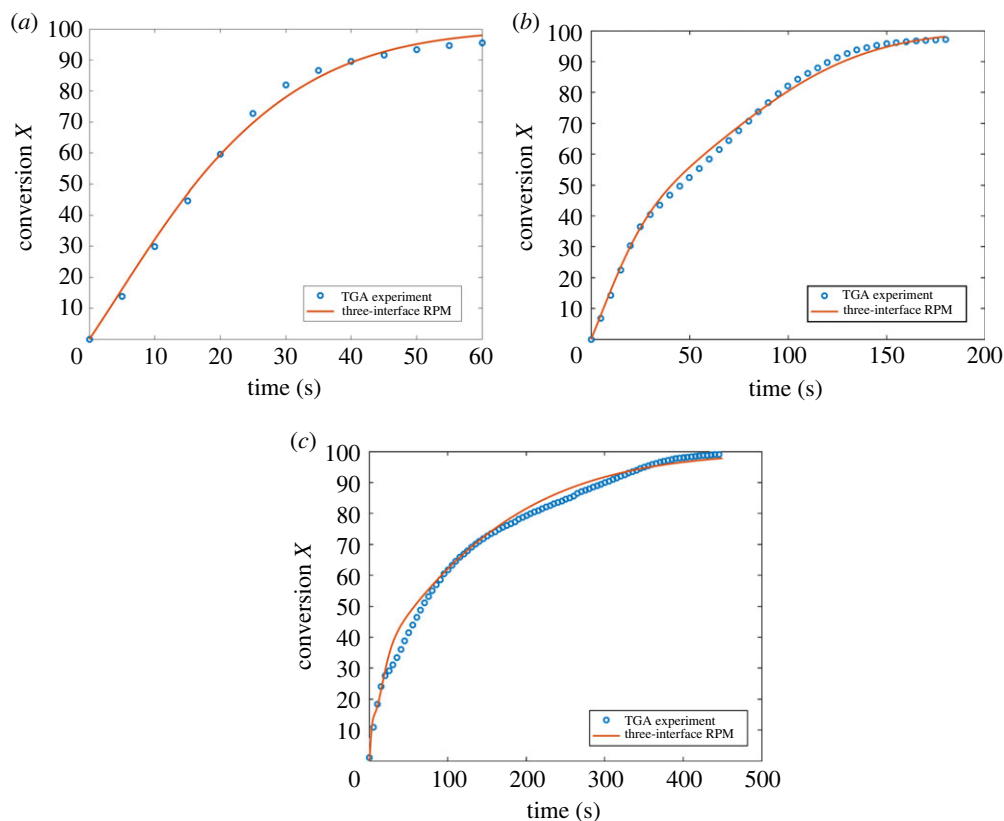
Figure 5. Example results of the three-interface RPM fitted to TGA experiments at 900°C. (*a*) Reduction from Fe_2O_3 to Fe_3O_4 under 3% CO and 15% CO_2 (balance N_2) gas concentrations. (*b*) Reduction from Fe_2O_3 to Fe_wO under 5% CO and 5% CO_2 (balance N_2) gas concentrations. (*c*) Reduction from Fe_2O_3 to Fe under 15% CO (balance N_2) gas concentrations.

input as initial parameter guesses for experiments at 5% CO and 5% CO_2, where thermodynamic equilibrium allows reduction from Fe_2O_3 to Fe_wO. This second fitting procedure yields rate constants $k_{s,2}$ and diffusion coefficients D_2. Figure 5*b* shows an example fit for Reaction 2 (R2) at $T = 900°C$. This procedure was repeated for the full reduction from Fe_2O_3 to Fe under 15% CO, yielding the rate constants $k_{s,3}$ and diffusion coefficients D_3. Figure 5*c* shows an example fit for Reaction 3 (R3) at $T = 900°C$. The chosen concentration ratios are based on the thermodynamic equilibrium data shown in figure 2 [48].

Unlike the original RPM or single layer shrinking core models, the three-interface RPM is able to capture changes in the rate of reaction that correspond to the depletion of higher oxidation states of iron oxide. For example, figure 5*b* shows a change in the gradient at approximately 40% conversion. This corresponds to the percentage mass loss of oxygen of the first reduction step from Fe_2O_3 to Fe_3O_4 within the overall reduction process from Fe_2O_3 to Fe_wO featured in the plot. The step change in the rate of reaction is characteristic of the reduction of iron oxides, where the first higher oxidation state depleted before the following reactions are complete. Similar rate changes are captured in the full reduction from Fe_2O_3 to Fe. The model also predicts a rate change caused by the depletion of Fe_2O_3 in figure 5*c*. The rate change here occurs at a lower percentage mass loss of oxygen (approx. 11.11%) because the fraction of the oxygen mass loss of the first reduction step compared with the total oxygen mass loss for the full reduction from Fe_2O_3 to Fe in figure 5*c* is less than that in figure 5*b* for the partial reduction from Fe_2O_3 to Fe_wO. There is also a second rate change due to the depletion of Fe_2O_3 and Fe_3O_4. Interestingly, the rate change here is somewhat overestimated by the three-interface RPM compared with the experiment results.
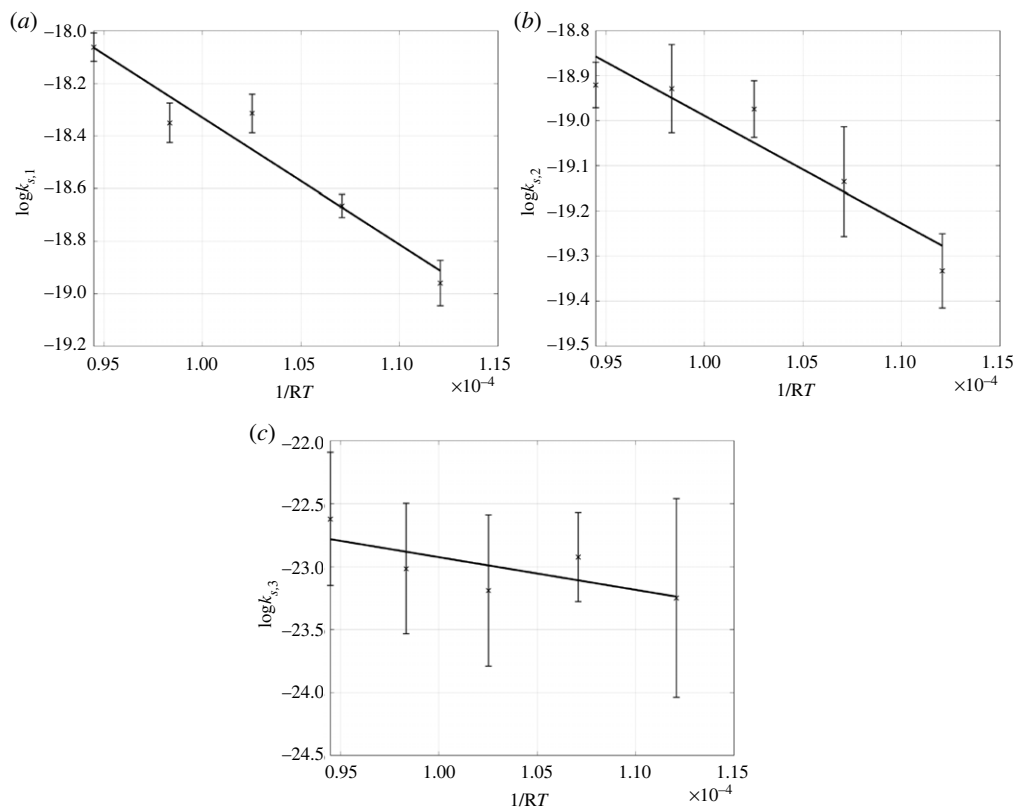
Figure 6. Arrhenius plots for all three reactions at temperatures between 800 and 1000°C. (*a*) Reaction 1 from Fe_2O_3 to Fe_3O_4. (*b*) Reaction 2 from Fe_3O_4 to Fe_wO. (*c*) Reduction from Fe_wO to Fe.

The experiments predict a rate change at approximately 30% conversion, which corresponds to the percentage of oxygen mass loss of the first two reduction steps. The three-interface RPM predicts a rate change at a slightly higher percentage oxygen mass loss. This is caused by the significant mass loss that can be attributed to the fact that the model includes contributions of the third reduction step in addition to the first two reduction steps. While the third reduction step is much slower than the first two, the percentage mass loss is large, since 70% of conversion is associated with the third reduction step. This could suggest that there is some resistance to the final reduction step beginning until the first two reduction steps, consuming Fe_2O_3 and Fe_3O_4, are fully complete. The reaction kinetics for the powders tested suggest that high metallization conversions are achievable in the order of seconds and minutes at only 15% concentration. Given the reduction kinetics of H_2 gas are even faster than CO gas [34], this suggests that next generation green hydrogen flash reduction processes being developed [11,12] are fundamentally feasible from a kinetics perspective.

Nonlinear least-squares fits of the model for all reduction processes (shown by example at 900°C in figure 5*a*–*c*) were successfully carried out across five temperatures between 800 and 1000°C, which are of interest in both iron and steelmaking and chemical looping applications [6,16]. Figure 6*b*,*c* depict Arrhenius plots for $k_{s,1}, k_{s,2}$ and $k_{s,3}$. Error bounds depicted indicate 95% confidence intervals for the parameter estimates. Figure 7 shows the Arrhenius plot for D_1. Interestingly, the fits for Reaction 2 and 3 were found to be insensitive to the diffusion coefficients D_2 and D_3. Extremely large confidence intervals were resultant for these two parameter estimates. The lower bounds were negative, which is unphysical. This implies that resistance to diffusion owed to D_2 and D_3 did not impact the model. These results suggest that Reaction 2 and 3
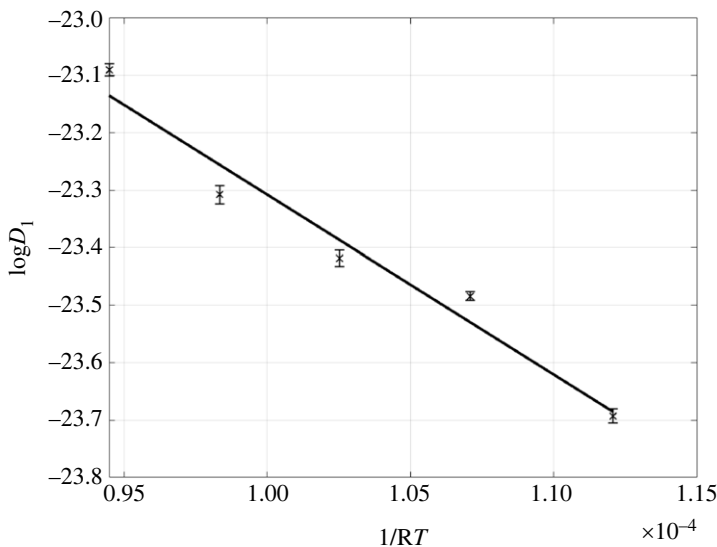
Figure 7. Arrhenius plot for the diffusion coefficient $D_1 = (1.72 \pm 20.2) \times 10^{-9} \exp((-31.3 \pm 31.3) \times 10^3/RT)$ for Reaction 1, Fe_2O_3 to Fe_3O_4.

Table 3. Random pore model rate constants for individual reactions in Arrhenius form.

CO/CO$_2$ ratio	rate constant $k_{s,i}/m^4\,mol^{-1}\,s^{-1}$
3%/15%	$k_{s,1} = (1.37 \pm 3.95) \times 10^{-6} \exp((-48.3 \pm 17.3) \times 10^3/RT)$
5%/5%	$k_{s,2} = (6.17 \pm 9.11) \times 10^{-8} \exp((-23.9 \pm 11.5) \times 10^3/RT)$
15%	$k_{s,3} = (1.48 \pm 23.6) \times 10^{-9} \exp((-25.9 \pm 33.5) \times 10^3/RT)$

are kinetically limited because the rate of diffusion is much faster than the rate of interfacial reaction. The error bounds are calculated based on the Jacobian, so the rate of change of the objective function with respect to the diffusion coefficient is very small, which leads to a very large confidence interval. Therefore, the model does not include (in any meaningful way) the diffusion coefficients D_2 or D_3. For Reaction 1, however, the Arrhenius plot for D_1 fits well to a straight line described by $D_1 = (1.72 \pm 20.2) \times 10^{-9} \exp((-31.3 \pm 31.3) \times 10^3/RT)$. The confidence intervals for both $k_{s,1}$ and D_1 are reasonable, which implies the reaction is under mixed control of both reaction and diffusion.

The kinetic constants and diffusion coefficient D_1 obtained by experiment fit well to straight line plots. The slope and intercept of each fitted line provide activation energies and frequency factors for each individual reaction are provided in Arrhenius form in table 3. As previously discussed, the diffusion coefficients D_2 and D_3 were not obtainable, suggesting the reactions were kinetically limited. While the model here describes gaseous diffusion across a porous product layer, the fact that D_1 limits the first reaction from hematite to magnetite and fits well to the Arrhenius expression supports recent work that extends the RPM to describe solid-state diffusion [15,17] for the reduction of iron oxides. The reason that solid-state diffusion coefficients follow the Arrhenius expression is that lattice diffusion occurs through interstitial mechanisms, and the prevalence of point vacancies increases with temperature in accordance with the Arrhenius expression [53,54]. It is still unclear what the dominant mechanism for diffusion is, since both gaseous diffusion modelling and solid-state diffusion appear to fit well to results. The true behaviour could be a mixture of both types of diffusion, depending on the initial particle properties and reaction conditions; this is an interesting area for future work in this field.
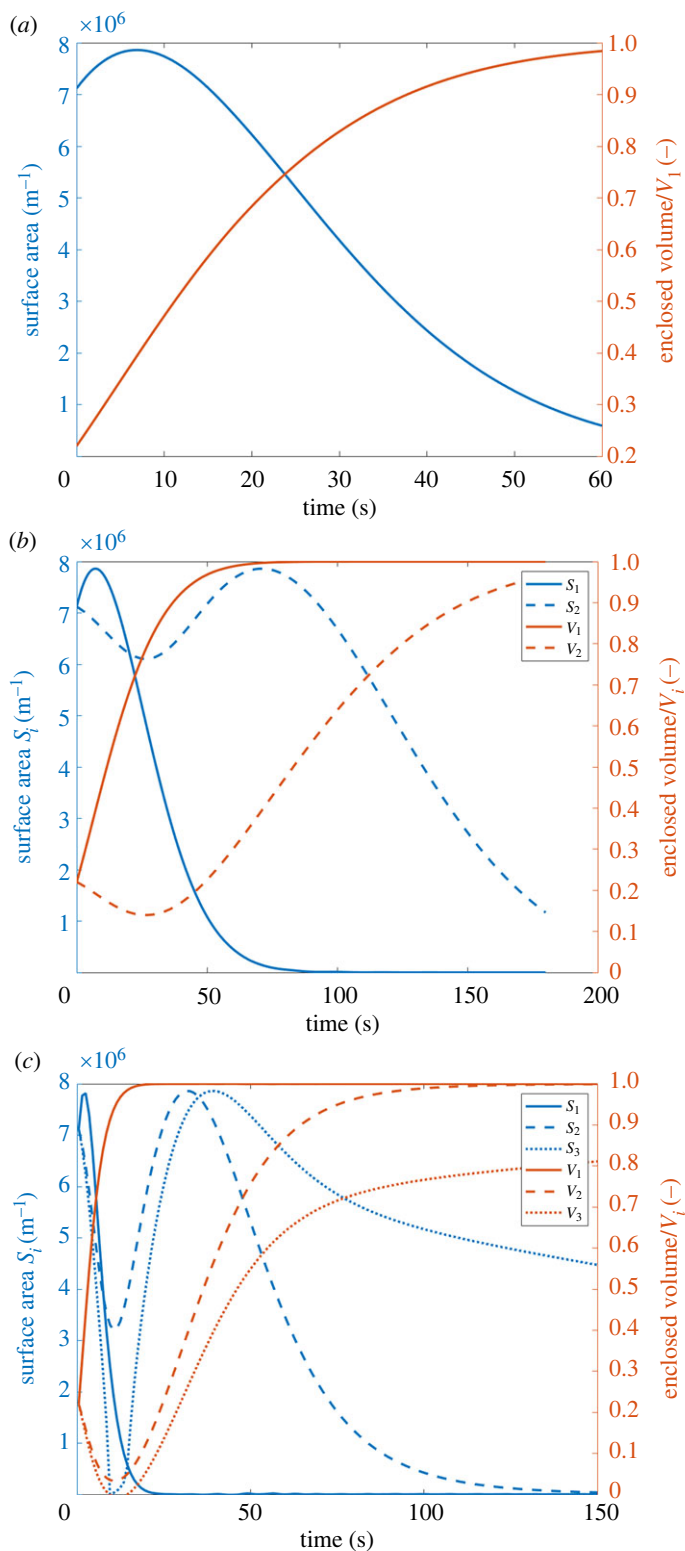
Figure 8. Interfacial surface area (S_i m^{-1}) for reaction at each interface and the enclosed volume V_i (—) of each interface over time at an example 900°C for (*a*) Reaction 1 from Fe_2O_3 to Fe_3O_4. (*b*) Reaction 1 and 2 from Fe_2O_3 to Fe_wO. (*c*) Reaction 1, 2 and 3 all the way from Fe_2O_3 to Fe.

To consider the plausibility of these results, the kinetic constants may be compared with the literature. In alignment with previous studies [16,17,33,34], the reduction from FeO to Fe is the slowest step, with rate constants an at least an order of magnitude slower than the preceding reactions.

Figure 8a–c shows the surface area for reaction at each interface and the enclosed volume by each interface over time predicted by the model at an example temperature $T = 900°C$.

Referring to figure 8a, the reactive surface areas increase to a maximum early in the reaction due to the expansion of small pores as the reactant is consumed. Later, however, the cylindrical pores begin to overlap with their neighbours, causing a reduction in the surface area. Since the reaction depicted is simply a single-step reduction, this result is mathematically identical to what is predicted by the original RPM. The maximum in surface area produces a rate maximum which is observed in some gas–solid reactions, including the system at hand [17,40,41]. More complex, coupled behaviour is observed in figure 8b,c, but can be understood by considering the growth dynamics and different molar volumes of each oxide layer. In figure 8b, where two reaction interfaces develop, the first reaction surface area initially grows and increases to a maximum, forming a product layer of Fe_3O_4 that has a greater molar volume than Fe_2O_3. This means that the second reaction interface initially decreases in surface area and enclosed volume. Eventually, however, as the first reaction slows and reaches completion, the second reaction dominates and the second reaction interface increases in surface area and reaches a maximum. This is once again characteristic of the RPM and is programmed by the statistics and nature of growing pores that intersect. Similar coupled behaviour is observed in figure 8c, but now with three simultaneous reactions proceeding at once. The results here also record RPM reaction rate constants for the intermediate reaction step between Fe_3O_4 to Fe_wO, which are at present unavailable in the literature, to the best of our knowledge.

5. Conclusion

The use of powders to enable fast reaction rates in next-generation reactor systems has attracted attention both in academia and industry. For example, there is interest in re-inventing iron production to reduce CO_2 emissions through the processing of iron ore fines, and also in chemical looping, a low energy penalty carbon capture technology where iron oxide powders are employed as oxygen carriers. This work has derived and experimentally tested a three-interface RPM for the gaseous reduction of iron oxides. It is suitable for small porous particles or porous powders where, in the case of iron oxide, three oxide layers develop. Characteristic of the original RPM, structural information about the particles of interest is able to be separated from kinetic and diffusion rates, including different molar volumes of each product layer. The model has incorporated experimentally measured parameters such as the initial surface area, porosity, pore size distribution. Furthermore, this model is able to describe simultaneous reduction all the way from Fe_2O_3 to Fe, and obtain individual rate constants of all three reactions from Fe_2O_3 to Fe_3O_4 (under mixed control, $k_{s,1} = 1.37 \times 10^{-6} \exp(-48.3 \times 10^3/RT)$, $D_1 = 1.72 \times 10^{-9} \exp(-31.3 \times 10^3/RT)$), Fe_2O_3 to Fe_wO (under kinetic control, $k_{s,2} = 6.17 \times 10^{-8} \exp(-23.9 \times 10^3/RT)$) and Fe_wO to Fe (under kinetic control $k_{s,3} = 1.48 \times 10^{-9} \exp(-25.9 \times 10^3/RT)$). The three-interface RPM developed in this paper extends the strength and reach of the original RPM to the gaseous reduction of iron oxide, an industrially relevant multi-layered gas–solid reaction system. Rates of metallization of the iron oxide powders were fast and promising for the innovation of green hydrogen-based flash DRI and chemical looping technologies.

Authors' contributions. J.J.W.: conceptualization, data curation, formal analysis, investigation, methodology, validation, writing—original draft; D.I.: writing—review and editing; N.S.: funding acquisition, project administration, supervision, writing—review and editing; P.S.F.: conceptualization, funding acquisition, methodology, project administration, supervision, validation, writing—review and editing.

All authors gave final approval for publication and agreed to be held accountable for the work performed therein.

References

1. Bahzad H. 2020 Chemical looping water splitting for hydrogen production, decarbonised steel production and energy storage/generation in-situ with carbon dioxide capture. PhD Thesis.
2. Kim J, Sovacool B, Bazilian M, Griffiths S, Lee J, Yang M, Lee J. 2022 Decarbonizing the iron and steel industry: a systematic review of sociotechnical systems, technological innovations, and policy options. *Energy Res. Soc. Sci.* **89**, 102565. (doi:10.1016/j.erss.2022.102565)
3. Spreitzer D, Schenk J. 2019 Reduction of iron oxides with hydrogen–a review. *Steel Res. Int.* **90**, 1900108. (doi:10.1002/srin.201900108)
4. Zhao J, Zuo H, Wang Y, Wang J, Xue Q. 2020 Review of green and low-carbon ironmaking technology. *Ironmaking Steelmaking* **47**, 296–306. (doi:10.1080/03019233.2019.1639029)
5. Sohn H, Mohassab Y. 2016 Development of a novel flash ironmaking technology with greatly reduced energy consumption and CO_2 emissions. *J. Sustain. Metall.* **2**, 216–227. (doi:10.1007/s40831-016-0054-8)
6. Bahzad H, Katayama K, Boot-Handford ME, Mac Dowell N, Shah N, Fennell PS. 2019 Iron-based chemical-looping technology for decarbonising iron and steel production. *Int. J. Greenhouse Gas Control* **91**, 102766. (doi:10.1016/j.ijggc.2019.06.017)
7. Fennell P, Driver J, Bataille C, Davis SJ. 2022 Cement and steel–nine steps to net zero. *Nature* **603**, 574–577. (doi:10.1038/d41586-022-00758-4)
8. Boot-Handford M *et al.* 2014 Carbon capture and storage update. *Energy Environ. Sci.* **7**, 130–189. (doi:10.1039/C3EE42350F)
9. Simpson A, Lutz AE. 2007 Exergy analysis of hydrogen production via steam methane reforming. *Int. J. Hydrogen Energy* **32**, 4811–4820. (doi:10.1016/j.ijhydene.2007.08.025)
10. Zhang X, Jiao K, Zhang J, Guo Z. 2021 A review on low carbon emissions projects of steel industry in the World. *J. Cleaner Prod.* **306**, 127259. (doi:10.1016/j.jclepro.2021.127259)
11. Barucchi A. 2022 Calix files a new patent for Zero Emissions Iron and steel - calix: Because Mars is for quitters.
12. Sohn H, Mohassab Y, Elzohiery M, Fan DQ. 2017 Status of the Development of Flash Ironmaking Technology. In *Applications of Process Engineering Principles in Materials Processing, Energy and Environmental Technologies*, pp. 15–23. New York, NY: Springer.
13. Zhang Z, Hills T, Scott S, Fennell P. 2016 Spouted bed reactor for kinetic measurements of reduction of Fe_2O_3 in a CO_2/CO atmosphere Part I: atmospheric pressure measurements and equipment commissioning. *Chem. Eng. Res. Des.* **114**, 307–320. (doi:10.1016/j.cherd.2016.06.028)
14. Jovanovic R, Marek E. 2021 Percolation theory applied in modelling of Fe_2O_3 reduction during chemical looping combustion. *Chem. Eng. J.* **406**, 126845. (doi:10.1016/j.cej.2020.126845)
15. Zhang Z, Wong JJ, Scott SA, Fennell PS. 2023 Spouted fluidised bed reactor for kinetic measurements of the reduction of Fe_2O_3 in a CO/CO_2 atmosphere part II: an extended random pore model for solid-state diffusion. *Chem. Eng. Res. Des.* **194**, 597–609. (doi:10.1016/j.cherd.2023.04.054)
16. Zhang Z, Yao J, Boot-Handford M, Fennell P. 2018 Pressurised chemical-looping combustion of an iron-based oxygen carrier: reduction kinetic measurements and modelling. *Fuel Process. Technol.* **171**, 205–214. (doi:10.1016/j.fuproc.2017.11.018)
17. Liu W, Lim JY, Saucedo M, Hayhurst AN, Scott SA, Dennis J. 2014 Kinetics of the reduction of Wüstite by hydrogen and carbon monoxide for the chemical looping production of hydrogen. *Chem. Eng. Sci.* **120**, 149–166. (doi:10.1016/j.ces.2014.08.010)
18. Yang F, Meerman J, Faaij A. 2021 Carbon capture and biomass in industry: a techno-economic analysis and comparison of negative emission options. *Renew. Sustain. Energy Rev.* **144**, 111028. (doi:10.1016/j.rser.2021.111028)
19. Leeson D, Dowell NM, Shah N, Petit C, Fennell P. 2017 A Techno-economic analysis and systematic review of carbon capture and storage (CCS) applied to the iron and steel, cement,

oil refining and pulp and paper industries, as well as other high purity sources. *Int. J. Greenhouse Gas Control* **61**, 71–84. (doi:10.1016/j.ijggc.2017.03.020)

20. Bui M *et al.* 2018 Carbon capture and storage (CCS): the way forward. *Energy Environ. Sci.* **11**, 1062–1176. (doi:10.1039/C7EE02342A)

21. Mukherjee S, Kumar P, Yang A, Fennell P. 2015 Energy and exergy analysis of chemical looping combustion technology and comparison with pre-combustion and oxy-fuel combustion technologies for CO_2 capture. *J. Environ. Chem. Eng.* **3**, 2104–2114. (doi:10.1016/j.jece.2015.07.018)

22. Fennell P, Anthony E. 2015 *Calcium and chemical looping technology for power generation and carbon dioxide* (CO_2) *capture*. Sawston, UK: Elsevier.

23. Adanez J, Abad A, Garcia-Labiano F, Gayan P, de Diego LF. 2012 Progress in chemical-looping combustion and reforming technologies. *Prog. Energy Combust. Sci.* **38**, 215–282. (doi:10.1016/j.pecs.2011.09.001)

24. Katayama K, Bahzad H, Boot-Handford M, Patzschke C, Fennell P. 2020 Process integration of chemical looping water splitting with a sintering plant for iron making. *Ind. Eng. Chem. Res.* **59**, 7021–7032. (doi:10.1021/acs.iecr.9b05945)

25. Pineau A, Kanari N, Gaballah I. 2007 Kinetics of reduction of iron oxides by H_2: part II. Low temperature reduction of magnetite. *Thermochim. Acta* **456**, 75–88. (doi:10.1016/j.tca.2007.01.014)

26. Sastri M, Viswanath R, Viswanathan B. 1982 Studies on the reduction of iron oxide with hydrogen. *Int. J. Hydrogen Energy* **7**, 951–955. (doi:10.1016/0360-3199(82)90163-X)

27. Moon IJ, Rhee C, Min D. 1998 Reduction of hematite compacts by H_2-CO gas mixtures. *Steel Res.* **69**, 302–306. (doi:10.1002/srin.199805555)

28. El-Geassy A, Nasr M. 1988 Influence of the original structure on the kinetics of hydrogen reduction of hematite compacts. *Trans. Iron Steel Inst. Jpn* **28**, 650–658. (doi:10.2355/isijinternational1966.28.650)

29. El-Geassy A. 1986 Gaseous reduction of Fe_2O_3 compacts at 600 to 1050°C. *J. Mater. Sci.* **21**, 3889–3900. (doi:10.1007/BF02431626)

30. Tsay Q, Ray W, Szekely J. 1976 The modeling of hematite reduction with hydrogen plus carbon monoxide mixtures: Part I. The behavior of single pellets. *AlChE J.* **22**, 1064–1072. (doi:10.1002/aic.690220617)

31. Valipour M, Hashemi MM, Saboohi Y. 2006 Mathematical modeling of the reaction in an iron ore pellet using a mixture of hydrogen, water vapor, carbon monoxide and carbon dioxide: an isothermal study. *Adv. Powder Technol.* **17**, 277–295. (doi:10.1163/156855206777213375)

32. Takenaka Y, Kimura Y, Narita K, Kaneko D. 1986 Mathematical model of direct reduction shaft furnace and its application to actual operations of a model plant. *Comput. Chem. Eng.* **10**, 67–75. (doi:10.1016/0098-1354(86)85047-5)

33. Negri E, Alfano OM, Chiovetta M. 1991 Direct reduction of hematite in a moving-bed reactor. Analysis of the water gas shift reaction effects on the reactor behavior. *Ind. Eng. Chem. Res.* **30**, 474–482. (doi:10.1021/ie00051a007)

34. Negri E, Alfano O, Chiovetta M. 1987 Direct reduction of hematite in a moving bed. Comparison between one- and three-interface pellet models. *Chem. Eng. Sci.* **42**, 2472–2475. (doi:10.1016/0009-2509(87)80122-7)

35. Chen F, Jiang T, Sohn H. 2015 Hydrogen reduction kinetics of hematite concentrate particles relevant to a novel flash ironmaking process. *Metall. Mater. Trans. B* **46**, 1133–1145. (doi:10.1007/s11663-015-0332-z)

36. Chen F, Mohassab Y, Zhang S, Sohn H. 2015 Kinetics of the reduction of hematite concentrate particles by carbon monoxide relevant to a novel flash ironmaking process. *Metall. Mater. Trans. B* **46**, 1716–1728. (doi:10.1007/s11663-015-0345-7)

37. Piotrowski K, Mondal K, Lorethova H, Stonawski L, Szymański T, Wiltowski T. 2005 Effect of gas composition on the kinetics of iron oxide reduction in a hydrogen production process. *Int. J. Hydrogen Energy* **30**, 1543–1554. (doi:10.1016/j.ijhydene.2004.10.013)

38. Szekely J. 2012 *Gas-solid reactions*. Cambridge, MA: Elsevier.

39. Ghadi A, Valipour M, Vahedi S, Sohn H. 2020 A review on the modeling of gaseous reduction of iron oxide pellets. *Steel Res. Int.* **91**, 1900270. (doi:10.1002/srin.201900270)

40. Bhatia S, Perlmutter D. 1980 A random pore model for fluid-solid reactions: I. Isothermal, kinetic control. *AlChE J.* **26**, 379–386. (doi:10.1002/aic.690260308)

41. Bhatia S, Perlmutter D. 1981 A random pore model for fluid-solid reactions: II. Diffusion and transport effects. *AlChE J.* **27**, 247–254. (doi:10.1002/aic.690270211)

42. Yao J, Zhang Z, Sceats M, Maitland G, Fennell P. 2017 Two-phase fluidized bed model for pressurized carbonation kinetics of calcium oxide. *Energy Fuels* **31**, 11 181–11 193. (doi:10.1021/acs.energyfuels.7b01384)
43. Scaltsoyiannes A, Antzaras A, Koilaridis G, Lemonidou A. 2021 Towards a generalized carbonation kinetic model for CaO-based materials using a modified random pore model. *Chem. Eng. J.* **407**, 127207. (doi:10.1016/j.cej.2020.127207)
44. Zhang J, Wang G, Zuo H. 2014 A modified random pore model for the kinetics of char gasification. *BioResources* **9**, 3497–3507. (doi:10.15376/biores.9.2.3497-3507)
45. Sangtong-Ngam K, Narasingha M. 2008 Kinetic study of Thai-lignite char gasification using the random pore model. *Sci. Technol. Asia* **13**, 16–26.
46. Song Q, Wang X, Gu C, Li H, Huo J. 2021 Study on CO_2 gasification kinetics of biomass char based on pore structure analysis: theoretical modelling of structural parameter ψ in random pore model. *Int. J. Energy Res.* **45**, 4429–4442. (doi:10.1002/er.6113)
47. Fei H, Hu S, Xiang J, Sun L, Fu P, Chen G. 2011 Study on coal chars combustion under O_2/CO_2 atmosphere with fractal random pore model. *Fuel* **90**, 441–448. (doi:10.1016/j.fuel.2010.09.027)
48. Barin I, Knacke O, Kubaschewski O. 2013 *Thermochemical properties of inorganic substances: supplement*. Berlin, Brandenburg, Germany: Springer Science & Business Media.
49. Fennell P, Dennis J, Hayhurst A. 2011 Latter stages of the reduction of NO to N_2 on particles of Fe while simultaneously oxidizing Fe to its oxides. *Energy & Fuels* **25**, 1510–1520. (doi:10.1021/ef101675j)
50. Avrami M. 1940 Kinetics of phase change. II transformation-time relations for random distribution of nuclei. *J. Chem. Phys.* **8**, 212–224. (doi:10.1063/1.1750631)
51. Patzschke C. 2018 Copper manganese oxides as oxygen carriers for chemical looping air separation for near-zero emission power generation. PhD Thesis.
52. Boot-Handford M. 2015 The Utilisation of Biomass as a fuel for Chemical Looping Combustion, PhD Thesis. Imperial College London.
53. Wagner C. 1952 Theoretical analysis of the diffusion processes determining the oxidation rate of alloys. *J. Electrochem. Soc.* **99**, 369. (doi:10.1149/1.2779605)
54. Heitjans P, Kärger J. 2006 *Diffusion in condensed matter: methods, materials, models*. Berlin, Brandenburg, Germany: Springer Science & Business Media.